

## Supplementary information

### Mechanistic Insights of Molecular Metal Polyselenides for Catalytic Hydrogen Generation

Alexander Elliott,<sup>‡</sup> James McAllister,<sup>‡</sup> Liudvika Masaityte, Mireia Segado Centellas, De-Liang Long, Alexey Ganin, Yu-Fei Song,<sup>\*</sup> Carles Bo<sup>\*</sup> and Haralampos N. Miras<sup>\*</sup>

#### Table of contents

Experimental Section.....	2
Computational details .....	3
Infrared spectroscopy.....	3
Raman spectroscopy .....	6
ESI - Mass spectroscopy .....	7
Powder x-ray data .....	8
<sup>77</sup> Se NMR spectroscopy .....	9
Crystal structure data .....	10
Electrochemistry.....	10
Comparison between DFT and crystal structures .....	13
DFT Benchmark calculations.....	13
DFT orbitals.....	14
DFT Protonation equilibria in non-reduced, single- and double- reduced forms .....	15
DFT HER mechanisms .....	20
Effect of electrode on energies .....	25

## Experimental Section

General experimental remarks: All chemicals were purchased from Sigma-Aldrich and used without further purification. All analyses were performed on a JASCO V-670 UV-Vis spectrometer, fitted with a JASCO EHC-716 temperature controller under nitrogen atmosphere.

**Synthesis of  $[\text{NMe}_4]_2[\text{Mo}_2\text{O}_2(\mu\text{-Se})_2(\text{Se}_2)_2]$  (1):** Elemental selenium (15.8 g, 200 mmol) is suspended in water (150 mL) and degassed by bubbling through nitrogen. The exhaust gas is passed through a bleach trap to destroy any hydrogen selenide produced. Sodium borohydride (9.46 g, 250 mmol) in water (150 mL), degassed by bubbling through nitrogen and added slowly to reduce the selenium, producing a dark red solution which is heated to 50°C for 40 minutes with stirring under a flow of nitrogen. This solution is then added to a degassed solution of ammonium heptamolybdate (8.85 g, 7.15 mmol) in water (175 mL) and stirred overnight under a flow of nitrogen. Black precipitate is removed by centrifugation, and the remaining liquid is filtered under gravity. Tetramethylammonium chloride (10 g, excess) is dissolved in a minimum amount of water and added to the solution to precipitate a dark brown solid  $[\text{NMe}_4]_2[\text{Mo}_2\text{O}_2\text{Se}_6]$  which is collected by vacuum filtration and washed with cold water, cold ethanol and diethyl ether. The material is used without further purification. For analysis the material is further purified by dissolution in acetonitrile and filtration, followed by removal of solvent under reduced pressure. Large crystals suitable could be grown by storing a saturated solution in DMF under a nitrogen atmosphere for several weeks. Yield: (82%, based on Mo). Anal. calcd for  $(\text{C}_{10}\text{H}_{27}\text{Mo}_2\text{N}_3\text{O}_2\text{Se}_6)$  Mr = 886.99): C, 13.54; H, 3.07; N, 4.74; Mo, 21.63. Found: C, 13.25; H, 2.92; N, 4.42; Mo, 22.02.

**Synthesis of  $[\text{NMe}_4]_2[\text{Mo}_2\text{O}_2(\mu\text{-Se})_2(\text{Se}_4)]_{0.5}[\text{Mo}_2\text{O}_2(\mu\text{-Se})_2(\text{Se}_2)(\text{Se}_3)]_{0.25}[\text{Mo}_2\text{O}_2(\mu\text{-Se})_2(\text{Se}_2)]_{0.25}$  (2):** Selenium powder (3.158 g, 40 mmol) was suspended in 40 mL water and attached to a bleach trap for exhaust gas. Sodium borohydride (3.027 g, 80 mmol) in 40 mL water is added slowly leading to a vigorous reaction to give a near colourless solution. A second portion of selenium powder (3.158 g, 40 mmol) is added and stirred for 15 minutes at room temperature before heating to 50 °C for 40 minutes to give a dark red solution of  $\text{Na}_2\text{Se}_2$ . 35 mL of this solution is added to a mixture of  $\text{MoO}_3$  (1.8 g, 14.3 mmol) and  $\text{Me}_4\text{NCl}$  (2.74 g, 25 mmol) in a hydrothermal Teflon-lined autoclave which is sealed and heated to 135 °C under autogenous pressure for 3 days then allowed to cool to room temperature. The resulting dark red crystalline material was then collected by vacuum filtration, washed with cold water and diethyl ether. The material was purified by dissolving in acetonitrile, filtering off undissolved material and then removing solvent by rotary evaporation. Single crystals were obtained by vapour diffusion with acetonitrile/diethyl ether for around 8 hours to avoid excessive degradation.

## Computational details

The Amsterdam Density Functional (ADF2017.1) software package was used in all the calculations. The GGA functional of Perdew, Burke and Ernzerhof with Grimme's empirical dispersion corrections (PBE-D3) was employed within the framework of the zeroth-order regular approximation (ZORA) quasi-relativistic Hamiltonian. A Slater-type orbital basis of triple zeta quality with two additional polarisation functions (TZ2P) was used for all the atoms keeping frozen core of  $1s^2$  for O,  $3s^23p^6$  for Se and  $3d^0$  for Mo. Implicit solvation effects in water were added in all calculations by applying the COSMO scheme with default parameters. No symmetry constraints were imposed in the geometry optimisations. Analytic vibrational frequencies were computed within the harmonic approximation, and thermodynamic corrections assuming ideal gas conditions at 298.15K and 1 atm. Cationic hydrogen addition steps were balanced with the calculated free energies of the Zundel cation ( $H_5O_2^+$ ) and two water molecules ( $2H_2O$ ). Absolute reduction potential of half-cell reactions were obtained from the free energies using the Nernst equation  $E^* = -\Delta G^\circ/(nF)$  ( $F$  = Faraday constant,  $n$  electron steps), and subsequently shifted relative to the normal hydrogen electrode (NHE) with the experimental absolute reduction potential  $E^*(NHE) = -4.24$  V such that  $E^\circ = E^*_{calc} - 4.24$ .

## Infrared spectroscopy

FT-IR spectra were collected in transmission mode using a Nicolet iS5 FTIR Spectrometer.

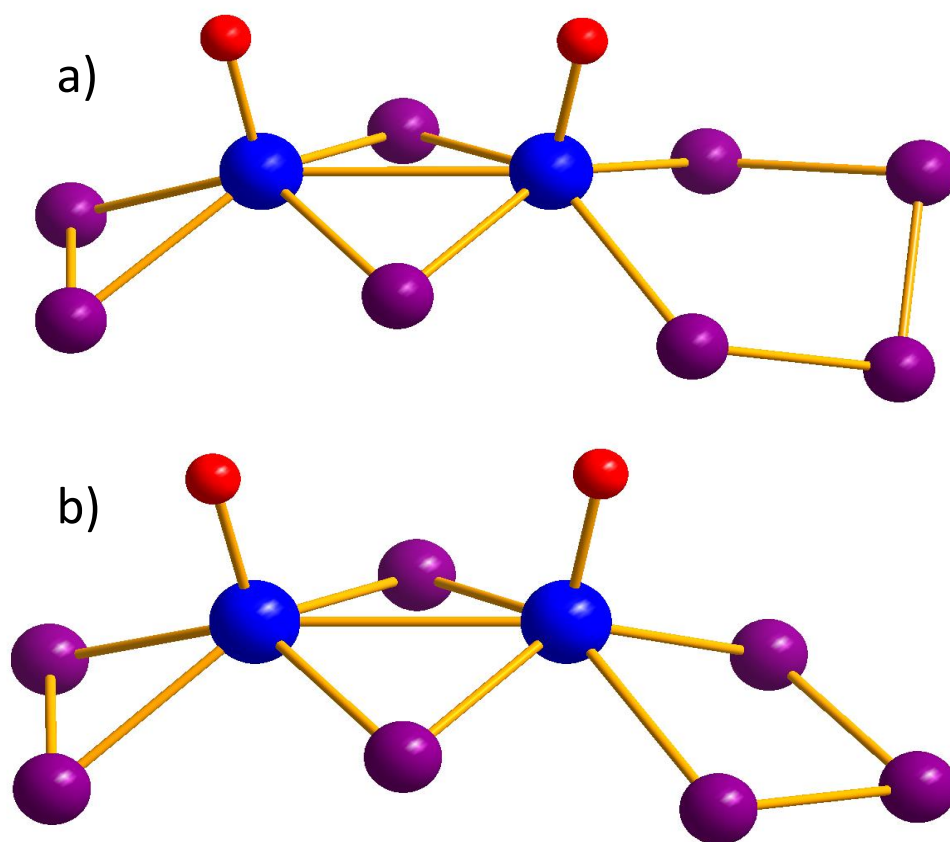


**Figure S1:** Crystal structure of a)  $[\text{Mo}_2\text{O}_2(\mu\text{-Se})_2(\text{Se}_2)(\text{Se}_4)]_2$  and b)  $[\text{Mo}_2\text{O}_2(\mu\text{-Se})_2(\text{Se}_2)(\text{Se}_3)]$  components of **2**. Mo, blue; Selenium, Purple; Oxygen, Red.

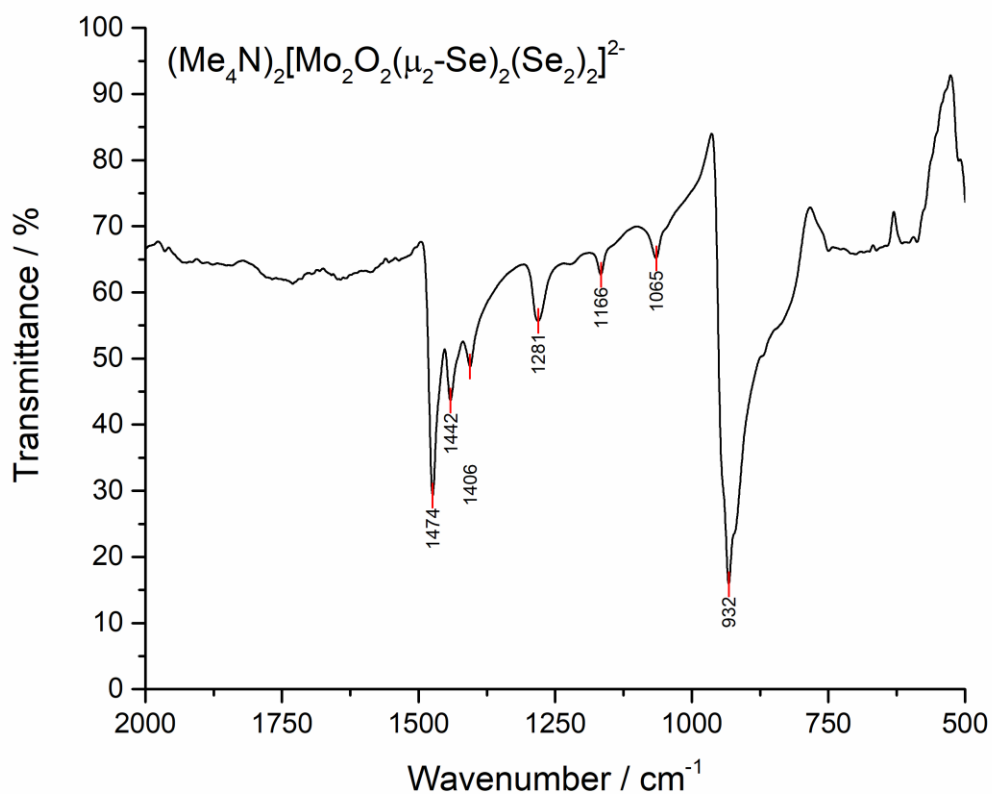


**Figure S2:** FT-IR spectra of **1**. Peaks located at 1474  $\text{cm}^{-1}$  (s), 1442  $\text{cm}^{-1}$  (w), 1406  $\text{cm}^{-1}$  (w), 1281  $\text{cm}^{-1}$  (w), 1166  $\text{cm}^{-1}$  (w), 1065  $\text{cm}^{-1}$  (w) and 932  $\text{cm}^{-1}$  (s). The strong peak at 1474  $\text{cm}^{-1}$  is assigned to  $\text{Me}_4\text{N}^+$  vibration and the strong peak at 932  $\text{cm}^{-1}$  is assigned to Mo=O vibration.

## Raman spectroscopy

Raman spectroscopy was carried out using a Horiba Jobin-Yvon LabRam HR800 equipped with a 532 nm laser. An aperture size of 100  $\mu\text{m}$  and a 1% filter was used in order to prevent sample degradation. The spectra were measured directly by focusing with a x50 microscope on the regions of GCE which contained the catalyst before and after cycling.

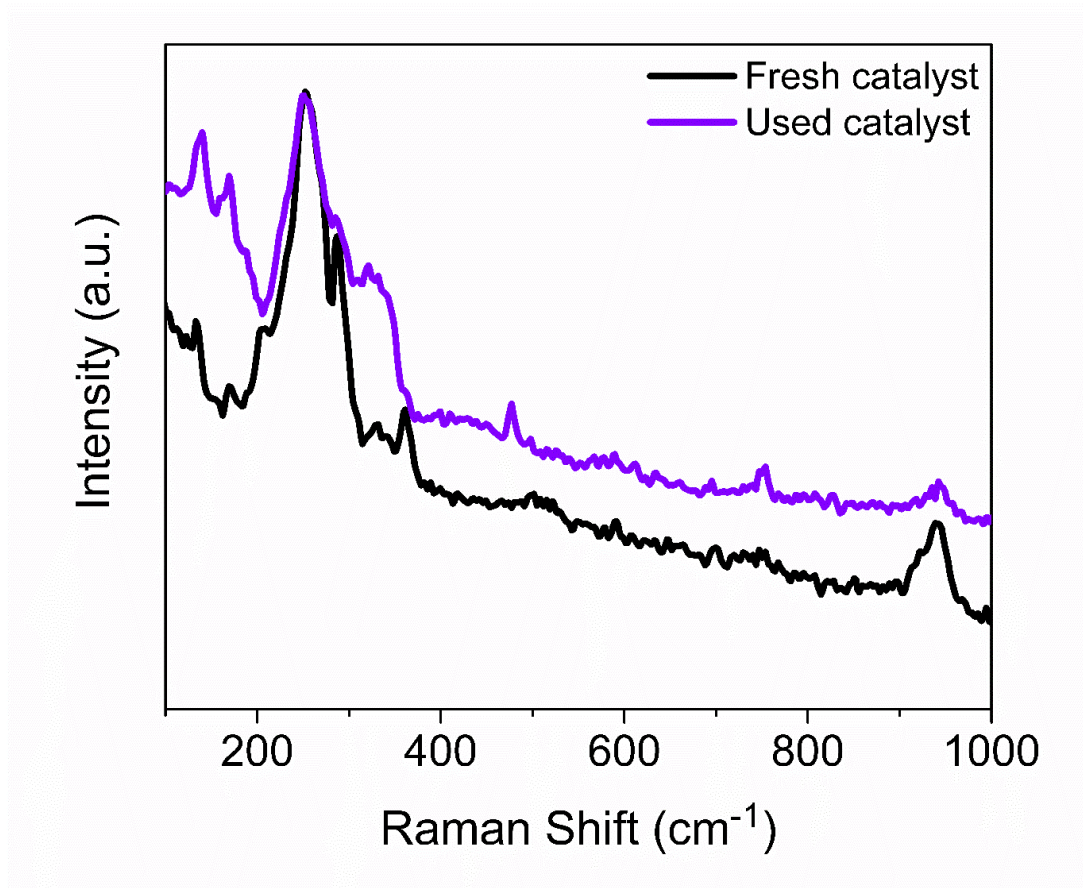


**Figure S3A:** Raman spectra of **1** before and after catalytic cycling (1000 cycles).

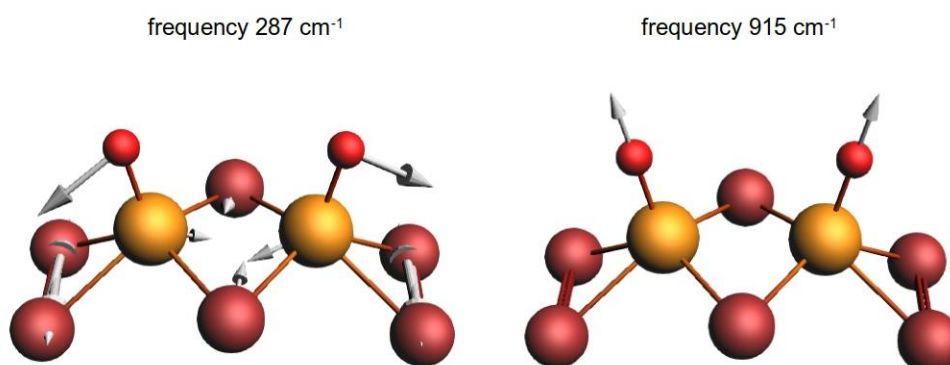


**Figure S3B.** DFT vibrational frequencies (cm<sup>-1</sup>) and displacements of the most intense Raman peaks of compound **1**.

## ESI - Mass spectroscopy

ESI-MS was performed using a Bruker MicrOTOF-Q quadrupole time-of-flight mass spectrometer. Samples were dissolved in acetonitrile introduced at a dry gas temperature of 180°C. The ion polarity for all MS scans recorded was negative, with the voltage of the capillary tip set at 4500 V, end plate offset at -500 V, funnel 1 RF at 400 Vpp and funnel 2 RF at 400 Vpp, hexapole RF at 200 Vpp, ion energy 5.0 eV, collision energy at 15 eV, collision cell RF at 1200 Vpp, transfer time at 120.0  $\mu$ s, the pre-pulse storage time at 15.0  $\mu$ s and analysed using the Bruker Daltonics v4.1 software.

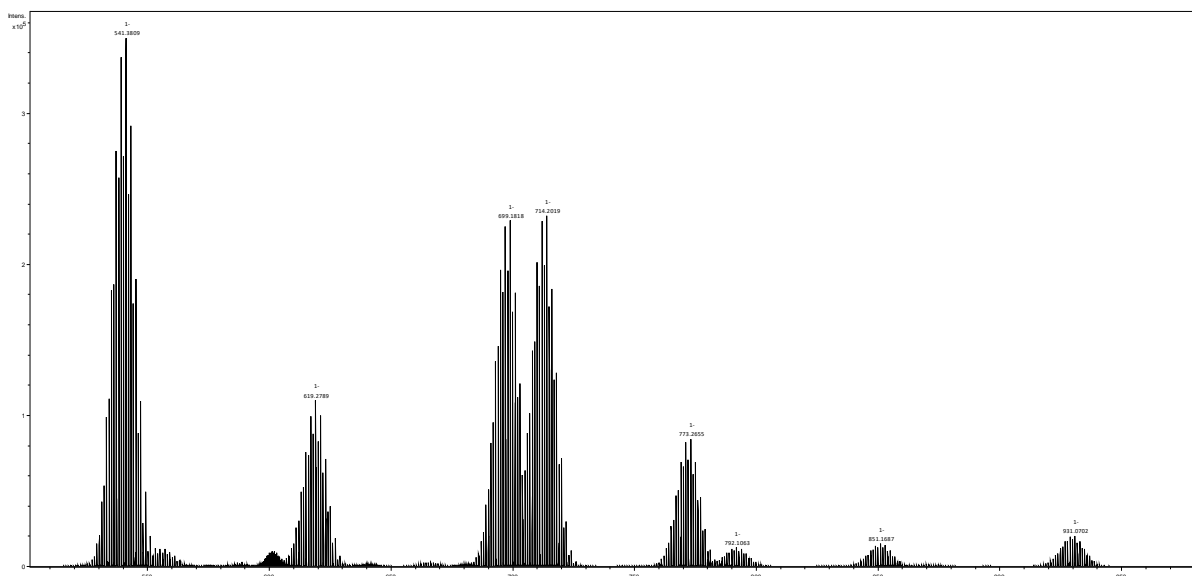


**Figure S4:** ESI-MS mass spectrum of  $(\text{Me}_4\text{N})_2[\text{Mo}_2\text{O}_2(\mu_2\text{-Se})_2(\text{Se}_2)_2]$  **1**. The observed envelopes centred at 981.07, 851.17, 773.27, 714.20, 699.18, 619.28, 541.38 are assigned to fragments  $[\text{Mo}_2\text{O}_2\text{Se}_8(\text{CH}_3\text{CN})_3\text{H}]^-$ ,  $[\text{Mo}_2\text{O}_2\text{Se}_7(\text{Me}_4\text{N})]^-$ ,  $[\text{Mo}_2\text{O}_2\text{Se}_6(\text{Me}_4\text{N})\text{H}]^-$ ,  $[\text{Mo}_2\text{O}_2\text{Se}_6\text{CH}_3]^-$ ,  $[\text{Mo}_2\text{O}_2\text{Se}_6\text{H}]^-$ ,  $[\text{Mo}_2\text{O}_2\text{Se}_5\text{H}]^-$  and  $[\text{Mo}_2\text{O}_2\text{Se}_4\text{H}]^-$  respectively. Derivative species are detected due to the ionization and consecutive ion-transfer process of the charged species.

## Powder x-ray data

The measurements were performed using a Panalytical Xpert-pro diffractometer with  $\text{CuK}\alpha$  radiation ( $\lambda=1.54178 \text{ \AA}$ ) operated in Bragg-Brentano geometry.

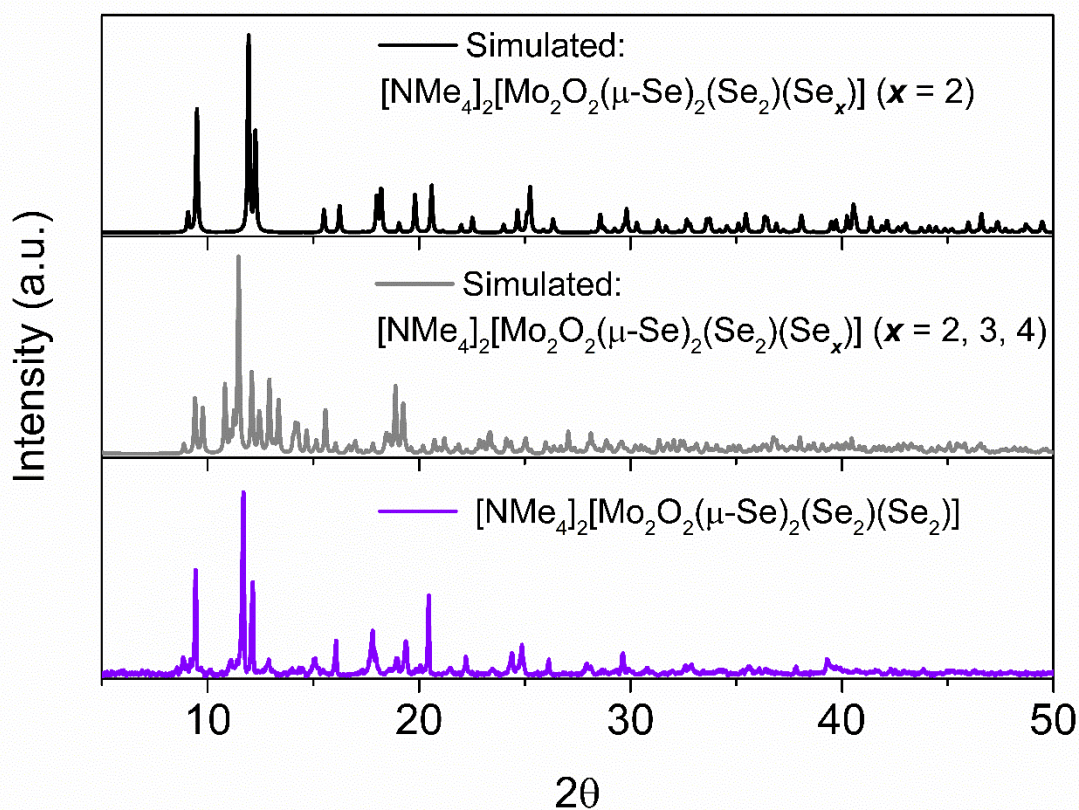


**Figure S5:** (Top) Simulated powder X-ray diffraction (PXR) pattern of  $(\text{Me}_4\text{N})_2[\text{Mo}_2\text{O}_2(\mu_2\text{-Se})_2(\text{Se}_2)_2]$ , (Middle) simulated PXR pattern of  $(\text{Me}_4\text{N})_2[\text{Mo}_2\text{O}_2(\mu_2\text{-Se})_2(\text{Se}_2)(\text{Se}_x)](x=2,3,4)$ , (Bottom) experimental PXR of as-synthesised  $(\text{Me}_4\text{N})_2[\text{Mo}_2\text{O}_2(\mu_2\text{-Se})_2(\text{Se}_2)_2]$ . The experimental pattern shows good agreement with the exclusively  $x=2$  structure. It is important to note that due to issues of preferred orientation the intensities of peaks in the experimental pattern will not necessarily match the predicted intensities.

## $^{77}\text{Se}$ NMR spectroscopy

NMR samples were prepared by dissolving 10 mg of purified **1** in 1 mL of dimethyl formamide, which is then filtered into an NMR tube which has been flushed with nitrogen to minimize denaturing. The spectra were recorded on a Bruker Avance III HD 600 spectrometer.

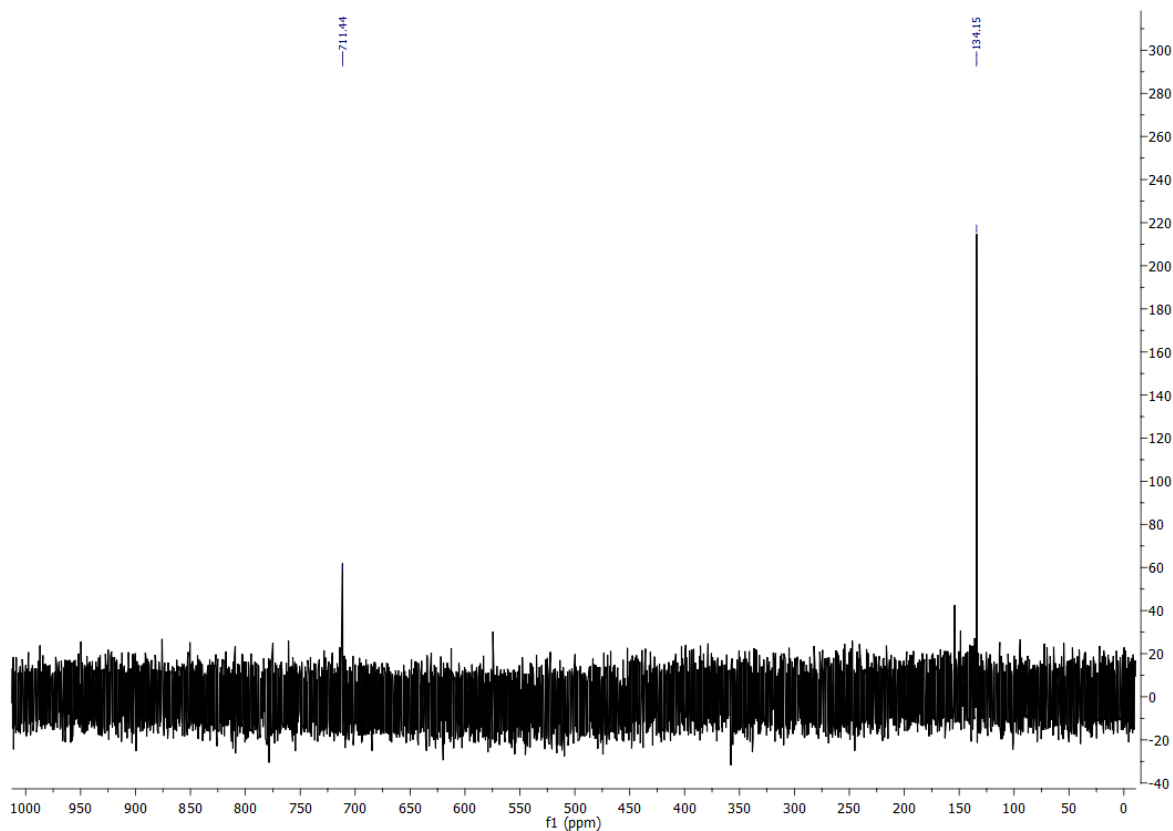


**Figure S6.**  $^{77}\text{Se}$  NMR spectra of **1** recorded in DMF. The spectrum shows two distinct peaks corresponding to the two unique environments in the dimer located at shifts of 134 ppm and 711 ppm relative to  $\text{Me}_2\text{Se}$ . The peak at 134 ppm is ascribed to the terminal  $\text{Se}_2^{2-}$  groups whilst the peak at 711 ppm is ascribed to the bridging  $\mu_2\text{-Se}^{2-}$  groups.

## Crystal structure data

Data were collected at 150(2) K using a Bruker AXS Apex II [ $\lambda(\text{MoK}\alpha)=0.71073 \text{ \AA}$ ] equipped with a graphite monochromator. Suitable single crystals were selected and mounted onto a rubber loop using Fomblin oil. Structure solution and refinement were carried out with SHELXS-97[citation] and SHELXL-97[citation] using the WinGX[citation] software package. Refinement was achieved by full-matrix least-squares on  $F^2$  via SHELXL-2013. Corrections for incident and diffracted beam absorption effects were applied using analytical methods. All non-hydrogen atom positions were refined anisotropically unless stated otherwise. Hydrogen atom positions were calculated using standard geometric criteria and refined using a riding model. All data manipulation and presentation steps were performed using WinGX.

## Electrochemistry

### Electrochemical measurements

Electrochemical measurements were made using a CH Instruments CHI760D potentiostat in a custom made three electrode electrochemical cell. 1M  $\text{H}_2\text{SO}_4$  (pH  $\sim 0$ ) was used as the electrolyte. The working electrode was a glassy carbon electrode (GCE) (BASi,  $d = 3.0 \text{ mm}$ ,  $A = 0.071 \text{ cm}^2$ ) onto which the catalyst under investigation had been deposited as described in the electrode preparation section. A graphite rod served as the counter electrode and an Ag/AgCl reference electrode (3 M NaCl, BASi). Before measurement the electrolyte and headspace were thoroughly degassed with Ar gas for 10 minutes. The electrode potentials can be converted to NHE according to the equation  $E(\text{NHE}) = E(\text{Ag/AgCl}) + 0.21 \text{ V}$ . The polarisation curves are measured by LSV with a scan rate of  $5 \text{ mV s}^{-1}$ . All measurements recorded have been  $iR$  corrected to compensate for electrolyte resistance. Tafel slopes were derived from the polarisation curves where the logarithm of the current density is plotted against the overpotential. Stability is measured under cyclic voltametric conditions between 0.21 and -0.16 V vs NHE with a scan rate of  $100 \text{ mV s}^{-1}$ .

### Electrode preparation

Working electrodes were prepared by depositing and drying a catalytic ink containing **(1)** on the surface of a glassy carbon electrode. Before applying the ink the surface of the electrode was polished to a mirror finish with an aqueous slurry of  $0.05 \text{ }\mu\text{m}$  alumina powder on a nylon polishing pad (Alvatek), followed by washing with deionised water. The electrode was then cleaned electrochemically by cyclic voltammetry at 1 to -1.2 V for 30 cycles at a scan rate of  $100 \text{ mV s}^{-1}$ .

Catalytic inks were prepared in DMF. The inks consisted of a combination of **(1)** and carbon powder (Cabot, Vulcan X72R) (2:1 ratio) in DMF (250  $\mu\text{L}$ ) and 5% Nafion solution (50  $\mu\text{L}$ ). The inks were

sonicated to give a homogenous mixture. 20  $\mu\text{L}$  portions were drop-cast on the GC electrode surface and dried at room temperature.

### Homogenous measurements

In order to verify the lack of electrochemical changes in the absence of protons cyclic voltammetry was performed on an aprotic homogenous solution consisting of 2 mg of  $[\text{Mo}_2\text{O}_2\text{Se}_6][\text{NMe}_4]_2$  dimer dissolved in 25 mL of acetonitrile with 0.1 M tetrabutylammonium tetrafluoroborate serving as the electrolyte. The same three electrode setup was used as for heterogenous measurements, using a clean, polished electrode. The region between 0 and -0.3 V (vs Ag/AgCl) was scanned, corresponding to the potentials at which reductive hydrogen waves are first evident in acidified aqueous solution. No increase in current compared to a blank measured in the absence of the catalyst was detected. When the scanned potential window is expanded the concentration is sufficient to observe electrochemical events related to structural changes at these more extreme potentials. On this basis we conclude that the catalyst is electrochemically inactive in the absence of protons at the mild potentials at which we report HER.

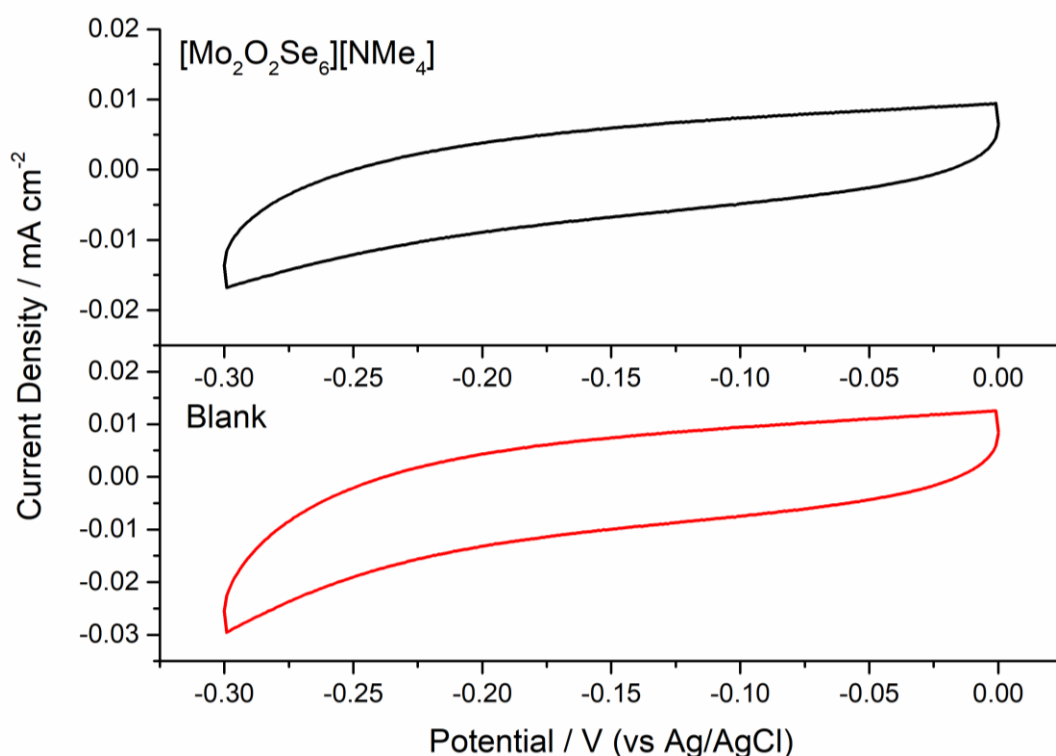


**Figure S7:** Homogenous measurements performed in acetonitrile; black, active catalyst (2 mg in 25 mL); red, blank.

## Gas Chromatography

A standard three-electrode electrochemical setup was used to perform bulk electrolysis over two hours using a working electrode prepared in the same manner as described earlier. 25 mL of 1 M  $\text{H}_2\text{SO}_4$  was used as the electrolyte. An airtight cell was used, which was degassed with Ar before the electrolysis was performed. A constant potential of -0.19 V (vs NHE) was applied and the charge passed was recorded. At 10 minute intervals 100  $\mu\text{L}$  volumes of the headspace were sampled and injected into an Agilent GC 7890A with thermal conductivity detector. The Faradaic efficiency was calculated as the ratio of expected  $\text{H}_2$  (%) in the headspace as calculated based on the charge passed to the  $\text{H}_2$  (%) detected by the GC based on the samples taken from the headspace. The turnover frequency (TOF) was calculated as the number of molecules of  $\text{H}_2$  present in the headspace divided by the number of molecules of catalyst present and the time elapsed. The number of catalytically active sites in a given material is unknown, calculations therefore take the entirety of the electrode material into account which will underestimate the theoretical TOF. Nevertheless, direct comparisons may be made so long as all TOF values are estimated in the same way.

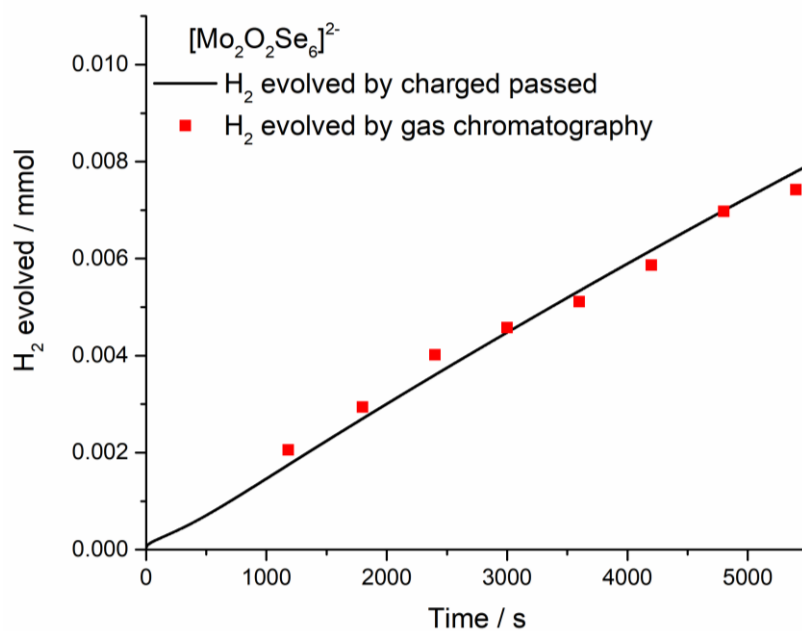


**Figure S8:** Hydrogen evolved over time determined by charge passed (black line) and gas chromatography (red squares)  $(\text{Me}_4\text{N})_2[\text{Mo}_2\text{O}_2(\mu_2\text{-Se})_2(\text{Se}_2)_2]$  deposited on glassy carbon electrode (bottom). The chromatograph response is reported as mmol  $\text{H}_2$  evolved based on a previous calibration.

## Comparison between DFT and crystal structures

**Table S1** Equilibrium distances of optimized DFT structures of compound 1  $\text{Mo}_2\text{O}_2(\mu\text{-Se})_2(\text{Se}_2)_2^{2-}$  and 2  $[\text{Mo}_2\text{O}_2(\mu\text{-Se})_2(\text{Se}_2)(\text{Se}_4)]^{4-}$ .

	Compound 1		Compound 2	
	DFT	Crystal	DFT	Crystal
d(Mo-Mo)	2.885	2.885	2.923	2.884
d(Mo-O)	2.923	2.884	1.709	1.687
d(Mo-Se <sub>μ</sub> )	2.473	2.447	2.476	2.461
d(Se-Se)	2.378	2.323	2.395	2.333

## DFT Benchmark calculations

We carried out some benchmark calculations to compare the GGA functional PBE (used in our previous work Nature Comm. 2019,10,370) with a high-level hybrid functional SAOP (J. Chem. Phys. 112, 1344 (2000)). The comparison between the two functionals is collected in Table S2, confirming same trends and conclusions of the HOMO-LUMO gap value for both functionals.

**Table S2** HOMO-LUMO gaps (in eV) for PBE and SAOP functionals with the TZ2P basis set.

	PBE	SAOP
$[\text{Mo}_2\text{O}_2(\mu\text{-S})_2(\text{S}_2)_2]^{2-}$	2.073	2.103
$[\text{Mo}_2\text{O}_2(\mu\text{-S})_2(\text{S}_2)(\text{S}_4)]^{4-}$	1.967	2.030
$[\text{Mo}_2\text{O}_2(\mu\text{-Se})_2(\text{Se}_2)_2]^{2-}$	1.785	1.807
$[\text{Mo}_2\text{O}_2(\mu\text{-Se})_2(\text{Se}_2)(\text{Se}_4)]^{4-}$	1.722	1.757

## DFT orbitals

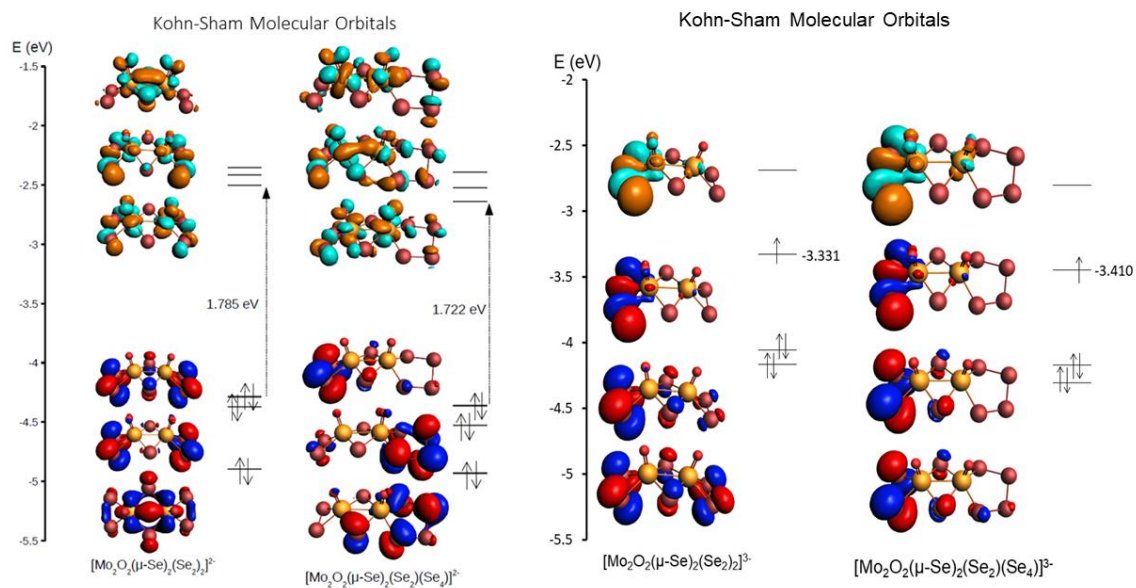


**Figure S9** Comparative molecular orbital analysis of  $\text{Mo}_2\text{O}_2(\mu\text{-Se})_2(\text{Se}_2)_2]^{2-}$  and  $[\text{Mo}_2\text{O}_2(\mu\text{-Se})_2(\text{Se}_2)(\text{Se}_4)]^{2-}$  as well as  $\text{Mo}_2\text{O}_2(\mu\text{-Se})_2(\text{Se}_2)_2]^{3-}$  and  $[\text{Mo}_2\text{O}_2(\mu\text{-Se})_2(\text{Se}_2)(\text{Se}_4)]^{3-}$

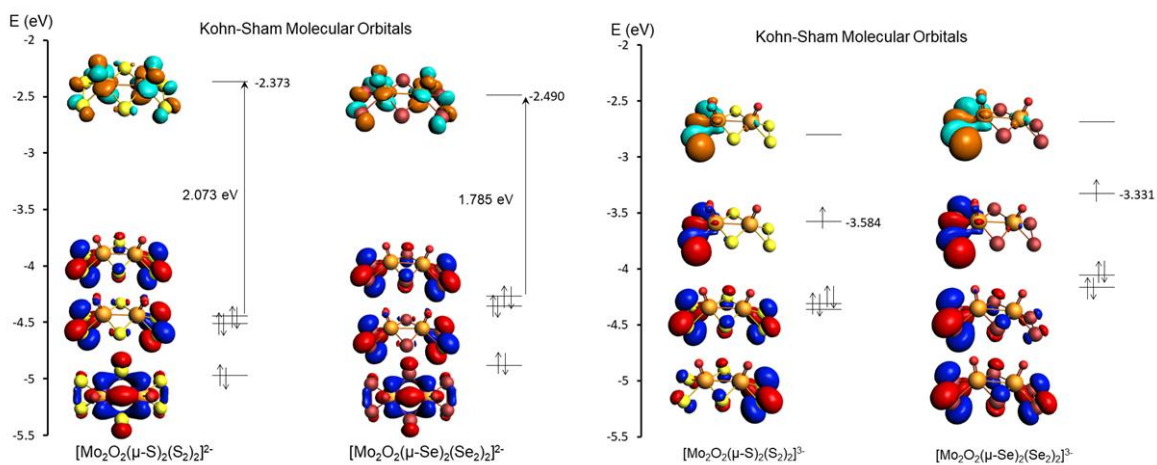


**Figure S10** Comparative molecular orbital analysis of the oxo-selenide and oxo-sulphide anions for 0 e- and 1e-.

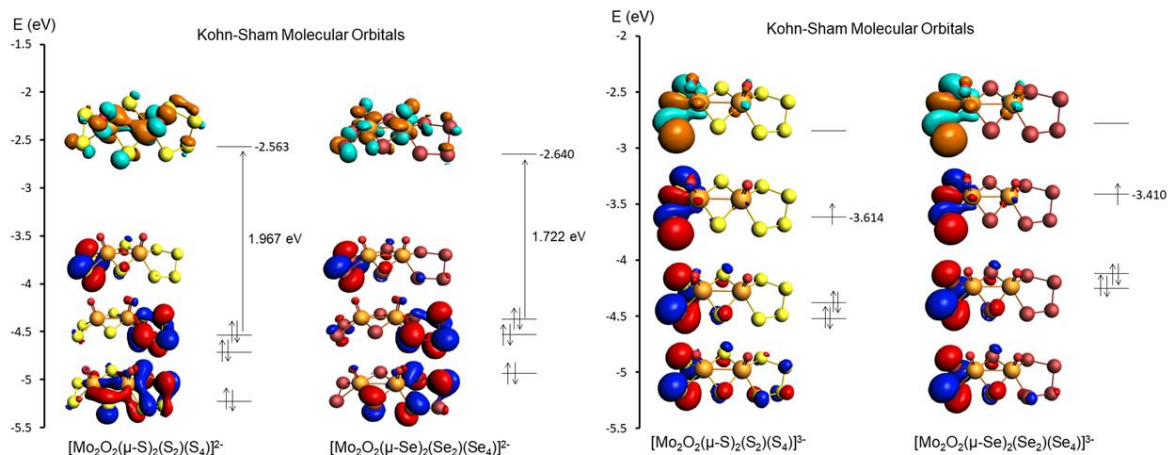


**Figure S11** Comparative molecular orbital analysis of the oxo-selenide and oxo-sulphide anions for 0 e- and 1e-.

DFT Protonation equilibria in non-reduced, single- and double- reduced forms

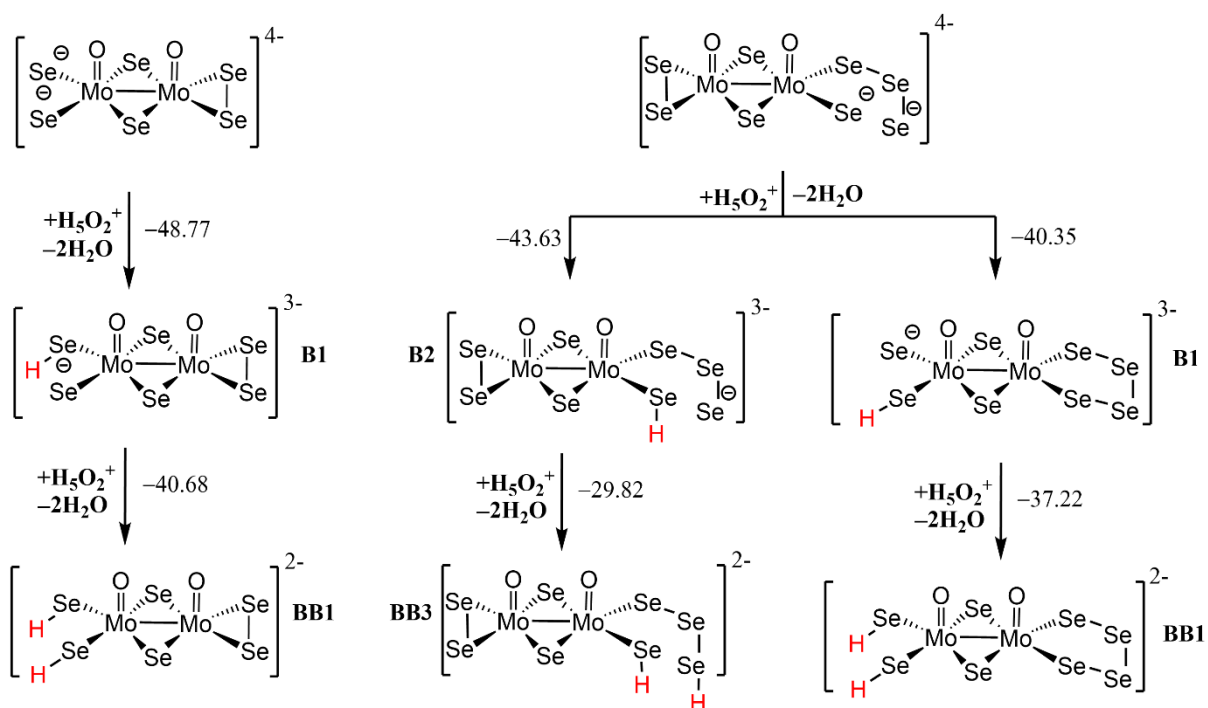


**Figure S12** Protonation equilibria of the  $[\text{Mo}_2\text{O}_2(\mu\text{-Se})_2(\text{Se}_2)(\text{Se}_x)]^{4-}$  ( $x = 2, 4$ )  $2e^-$  reduced species. Free energies in kcal·mol<sup>-1</sup>.

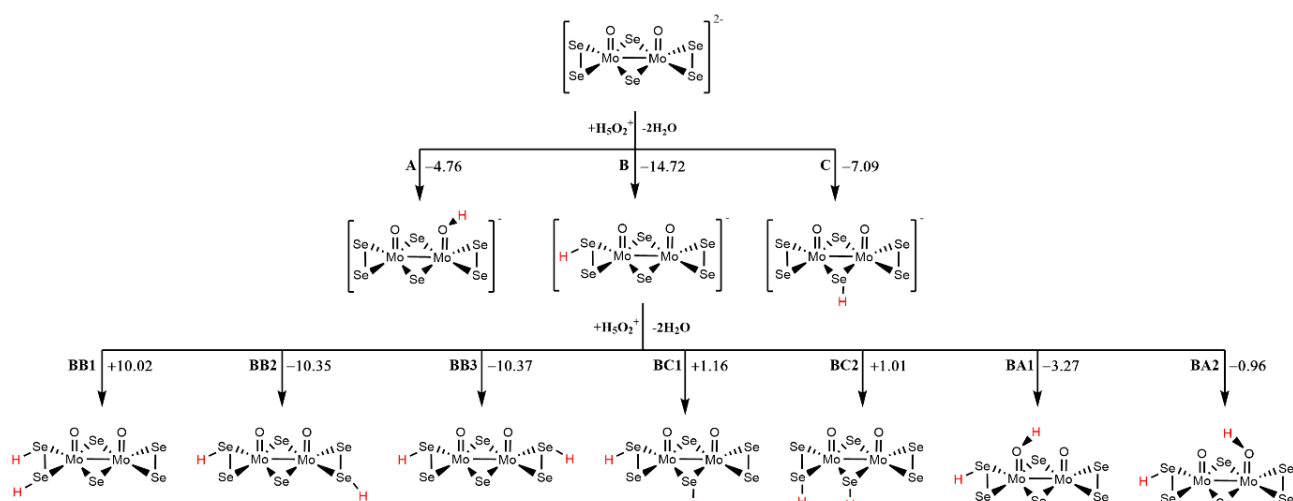


**Figure S13** Protonation genealogy of compound  $\text{Mo}_2\text{O}_2(\mu\text{-Se})_2(\text{Se}_2)_2]^{2-}$  without any added electrons. Listed values are free energies in aqueous solution in  $\text{kcal}\cdot\text{mol}^{-1}$

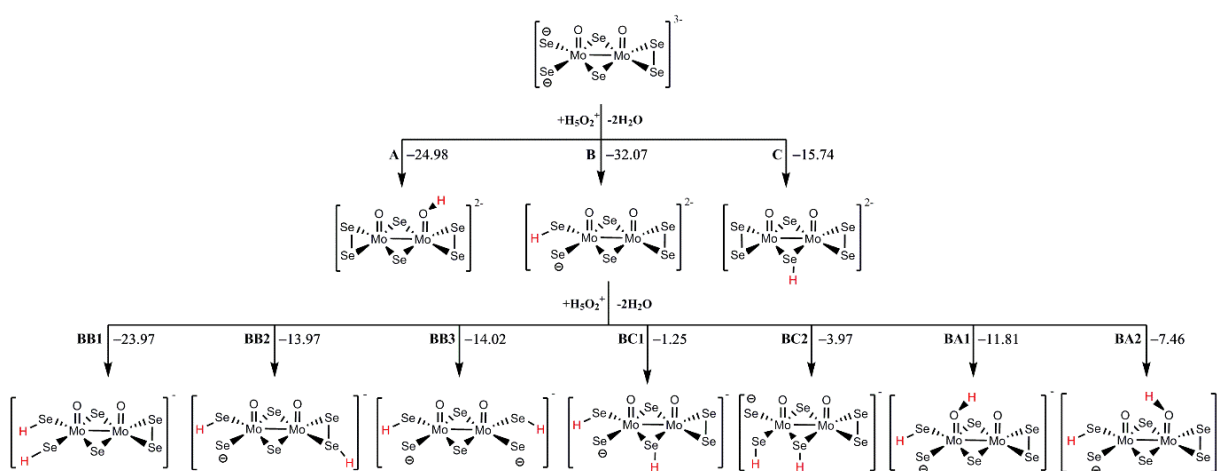


**Figure S14** Protonation genealogy of singly reduced compound  $\text{Mo}_2\text{O}_2(\mu\text{-Se})_2(\text{Se}_2)_2]^{3-}$ . Listed values are free energies in aqueous solution in  $\text{kcal}\cdot\text{mol}^{-1}$

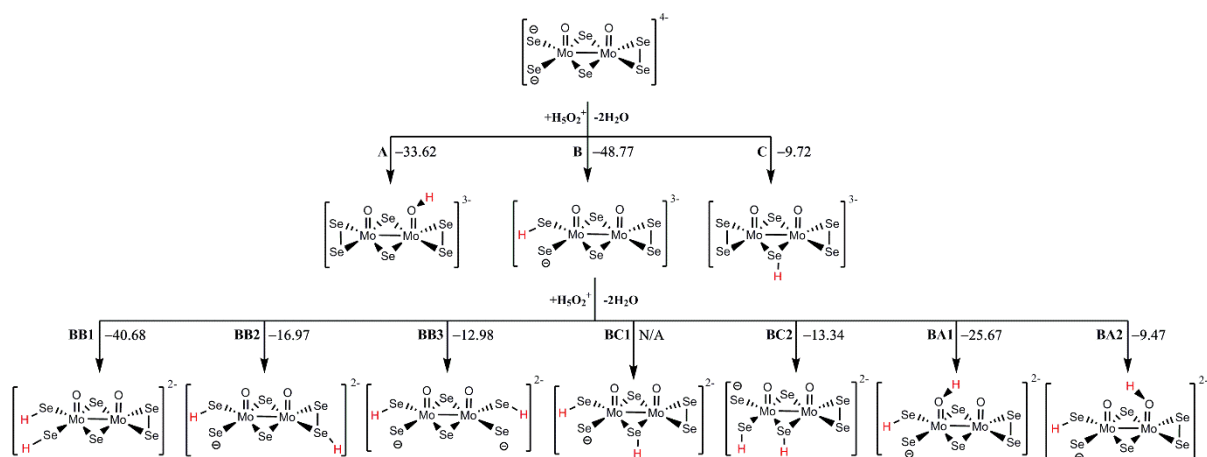


**Figure S15** Protonation genealogy of doubly reduced compound  $\text{Mo}_2\text{O}_2(\mu\text{-Se})_2(\text{Se}_2)_2^{4-}$ . Listed values are free energies in aqueous solution in  $\text{kcal}\cdot\text{mol}^{-1}$

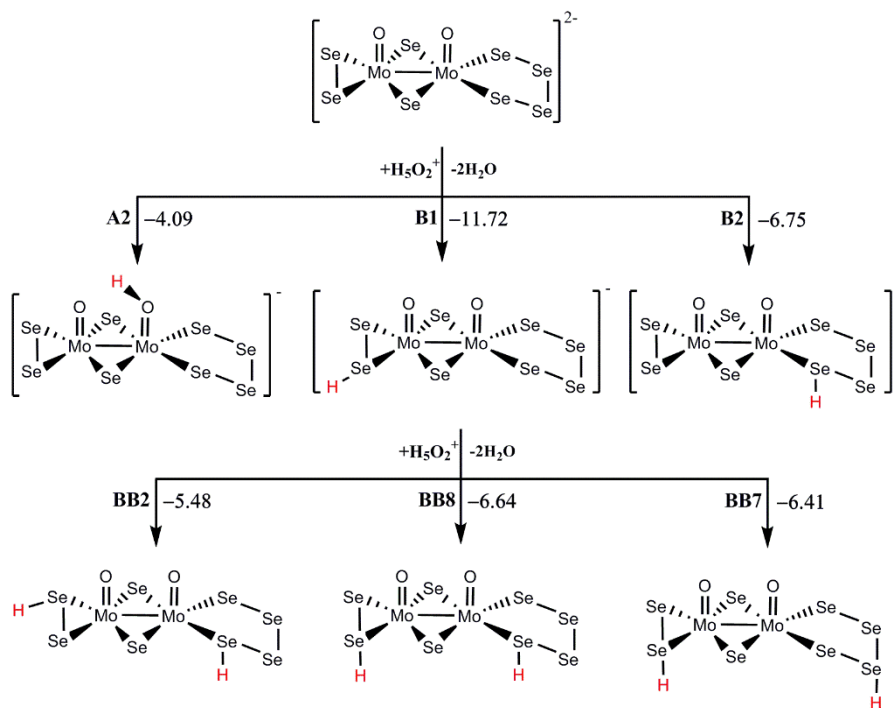


**Figure S16** Protonation genealogy of compound  $[\text{Mo}_2\text{O}_2(\mu\text{-Se})_2(\text{Se}_2)(\text{Se}_4)]^{2-}$  without any added electrons. Listed values are free energies in aqueous solution in  $\text{kcal}\cdot\text{mol}^{-1}$ . Since selenium analogues have been following the trends of their sulphur analogues, only the most probable structures are displayed.

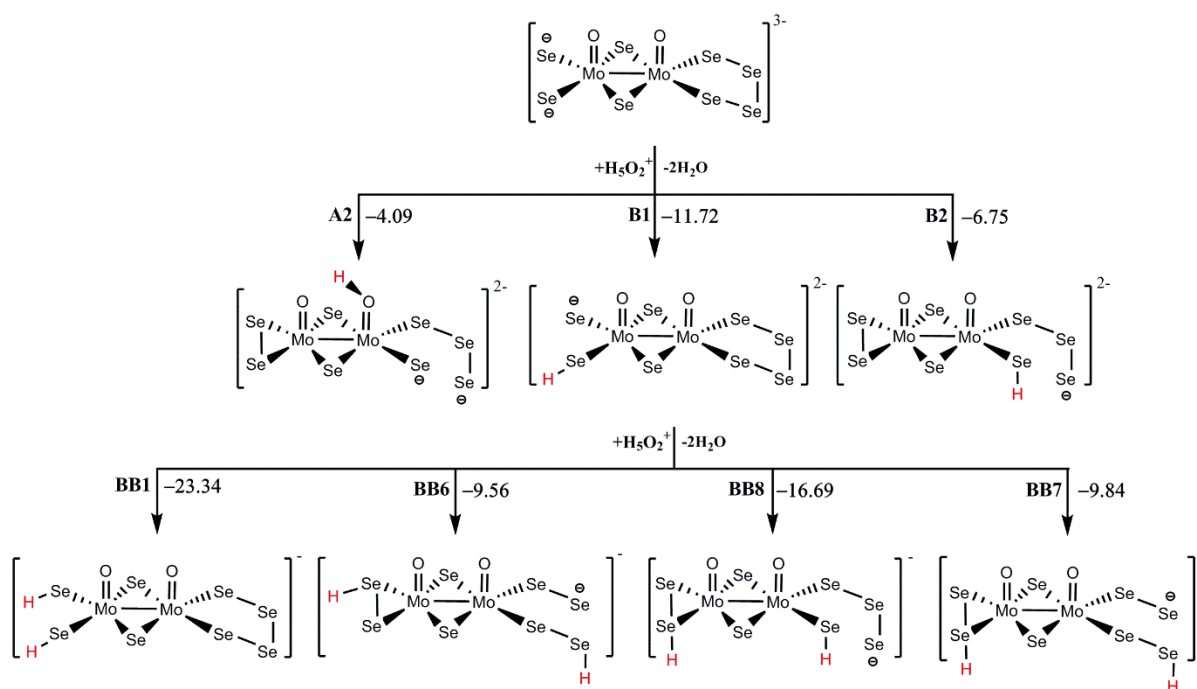


**Figure S17** Protonation genealogy of singly reduced compound  $[\text{Mo}_2\text{O}_2(\mu\text{-Se})_2(\text{Se}_2)(\text{Se}_4)]^{3-}$ . Listed values are free energies in aqueous solution in  $\text{kcal}\cdot\text{mol}^{-1}$ . Since selenium analogues have been following the trends of their sulphur analogues, only the most probable structures are displayed.

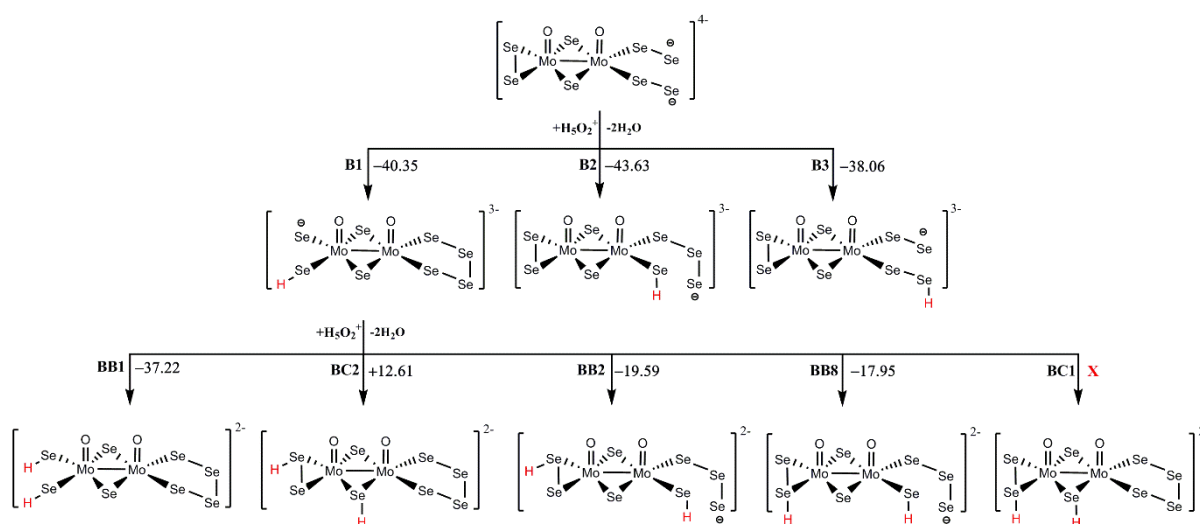


**Figure S18** Protonation genealogy of doubly reduced compound  $[\text{Mo}_2\text{O}_2(\mu\text{-Se})_2(\text{Se}_2)(\text{Se}_4)]^{4-}$ . Listed values are free energies in aqueous solution in  $\text{kcal}\cdot\text{mol}^{-1}$ . Since selenium analogues have been following the trends of their sulphur analogues, only the most probable structures are displayed.

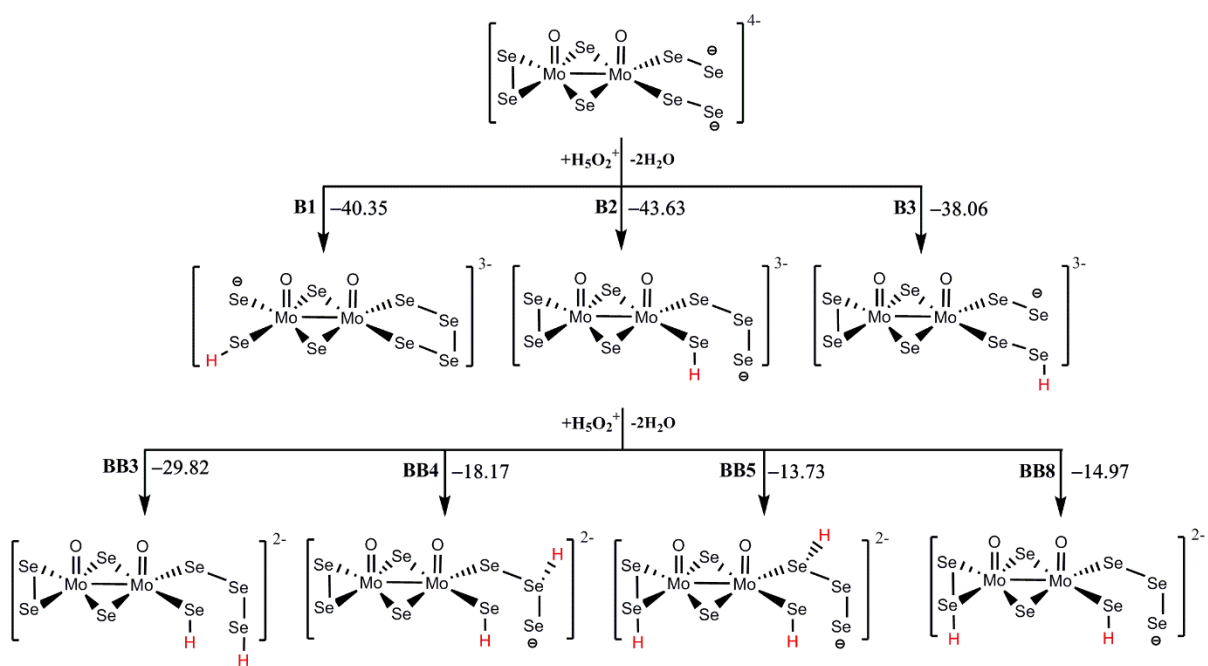


**Figure S19** Protonation genealogy of doubly reduced compound  $[\text{Mo}_2\text{O}_2(\mu\text{-Se})_2(\text{Se}_2)(\text{Se}_4)]^{2-}$ . Listed values are free energies in aqueous solution in  $\text{kcal}\cdot\text{mol}^{-1}$ . Since selenium analogues have been following the trends of their sulphur analogues, only the most probable structures are displayed.

## DFT HER mechanisms

Taffel and Heyrovsky HER mechanisms were studied by optimizing the geometry of the transition states of the molecular hydrogen forming steps. Figure 3 in the main manuscript shows the most important thermodynamic routes as function of two variables: electron addition and proton addition. Moreover, a complete study of all possible single- and double protonated isomers for  $0e^-$ ,  $1e^-$  and  $2e^-$  species are depicted in figures S12 to S18. In all cases the most thermodynamical species are the double-protonated forms. Based on the computed reduction potentials, two electron addition to double-protonated non-reduced species is a non-favourable process. In contrast, reduction reactions are more favourable from single protonated and non-protonated forms.

We consider that both Taffel and Heyrovsky mechanisms start from double reduced species. In the case of Heyrovsky mechanism, single- and double- protonated species were considered. In the case of Taffel mechanism, hydrogen evolution is only possible from double-protonated forms. More details for the intermediates used in the study can be found in the lines below.

**[Mo<sub>2</sub>O<sub>2</sub>(μ-Se)<sub>2</sub>(Se<sub>2</sub>)<sub>2</sub>]<sup>4-</sup> species:** Heyrovsky mechanism from single-protonated B1 (See figure 4 main text) and from double- protonated BB1 (Figure S19). Taffel mechanism from double-protonated forms, from BB1 intermediate where two sulfurs are protonated (Figure S20) and from BA1 where one sulfur and one oxygen are protonated (Figure S21).

The results show that the most favourable reaction is the Heyrovsky reaction mechanism. The reaction profile of single-protonated B1 has the lowest energy barrier with a value of 2.58 kcal/mol. In the case of Taffel reaction mechanism, BA1 reaction profile has the lowest activation Gibbs energy of 37.45 kcal/mol, but BB1 is the most thermodynamically stable intermediate.

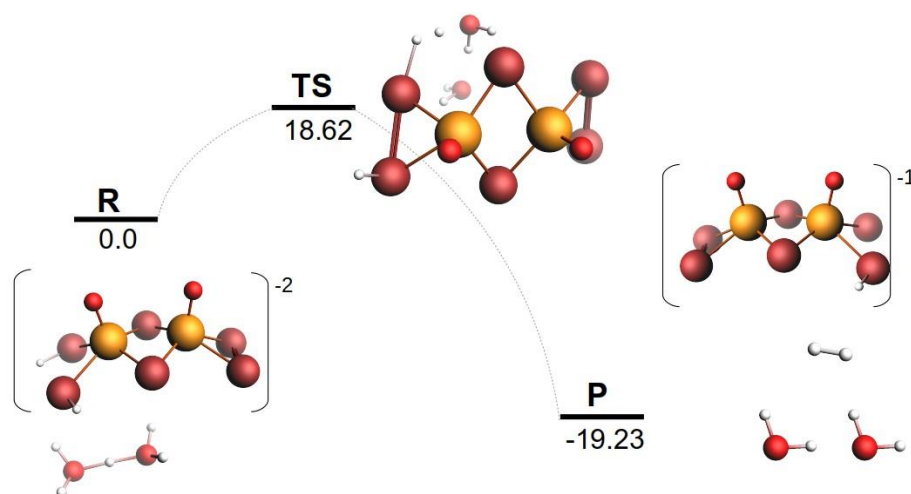


**Figure S20** Gibbs reaction profile for **Heyrovsky reaction** mechanism from intermediate **BB1**  $H_2[Mo_2O_2(\mu-Se)_2(Se_2)_2]^{2-}$  and  $H_5O_2^+$  to B1  $H[Mo_2O_2(\mu-Se)_2(Se_2)_2]^{1-}$  and  $H_2$ .

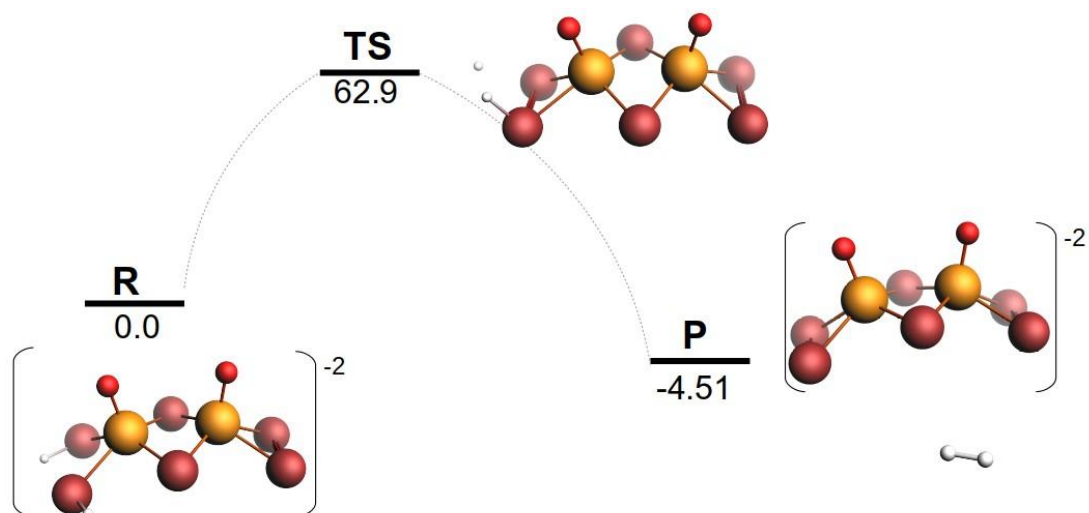


**Figure S21** Gibbs reaction profile for **Taffel reaction** mechanism from intermediate **BB1**  $\text{H}_2[\text{Mo}_2\text{O}_2(\mu\text{-Se})_2(\text{Se}_2)_2]^{2-}$  to  $[\text{Mo}_2\text{O}_2(\mu\text{-Se})_2(\text{Se}_2)_2]^{2-}$  and  $\text{H}_2$ .

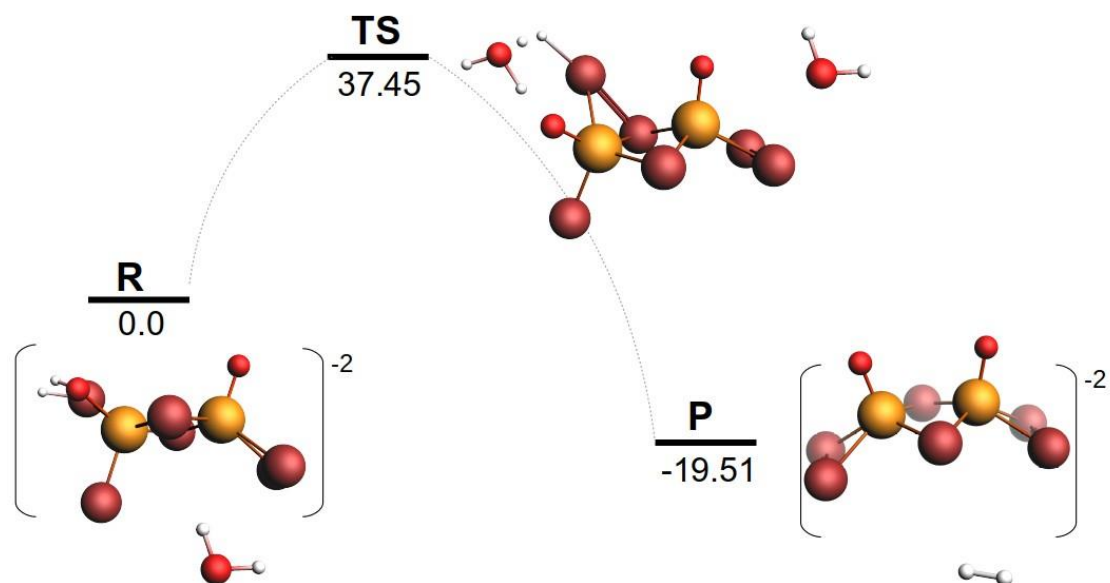
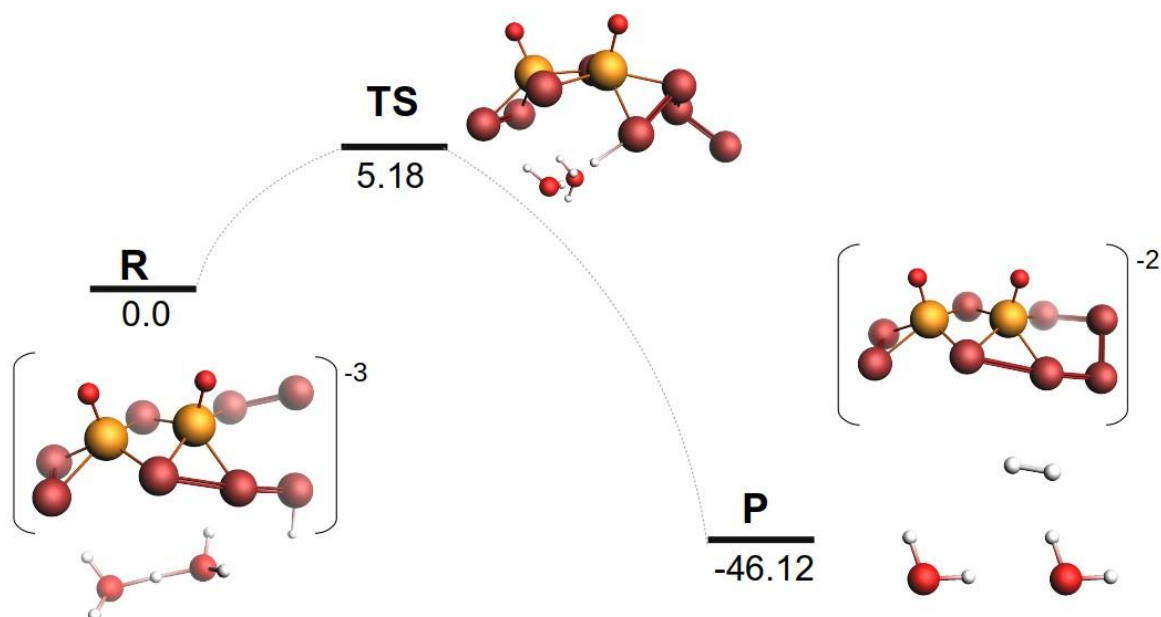


**Figure S22** Gibbs reaction profile for **Taffel reaction** mechanism from intermediate **BA1**  $\text{H}_2[\text{Mo}_2\text{O}_2(\mu\text{-Se})_2(\text{Se}_2)(\text{Se}_4)]^{2-}$  and  $\text{H}_2\text{O}$  to  $[\text{Mo}_2\text{O}_2(\mu\text{-Se})_2(\text{Se}_2)(\text{Se}_4)]^{2-}$  and  $\text{H}_2$ .

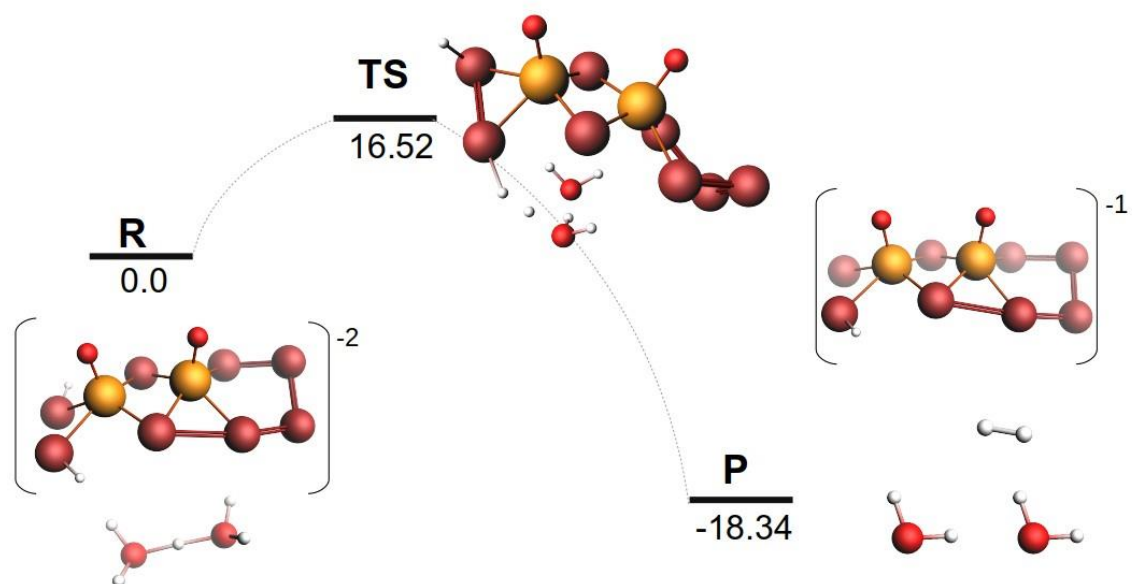
**$[\text{Mo}_2\text{O}_2(\mu\text{-Se})_2(\text{Se}_2)(\text{Se}_4)]^{4-}$  species:** : Heyrovsky mechanism from single-protonated B3 where the proton is in the 4-member ring (Figure S22); from double-protonated BB1 where the two protons are in 2-ring (this structure is chosen for the study in order to compare with  $[\text{Mo}_2\text{O}_2(\mu\text{-Se})_2(\text{Se}_2)_2]^{4-}$

specie , Figure S23); from double- protonated BB3 where the two protons are in the 4-ring (Figure S24). Tafel mechanism is only computed from BB1 at double-protonated forms (Figure S25).

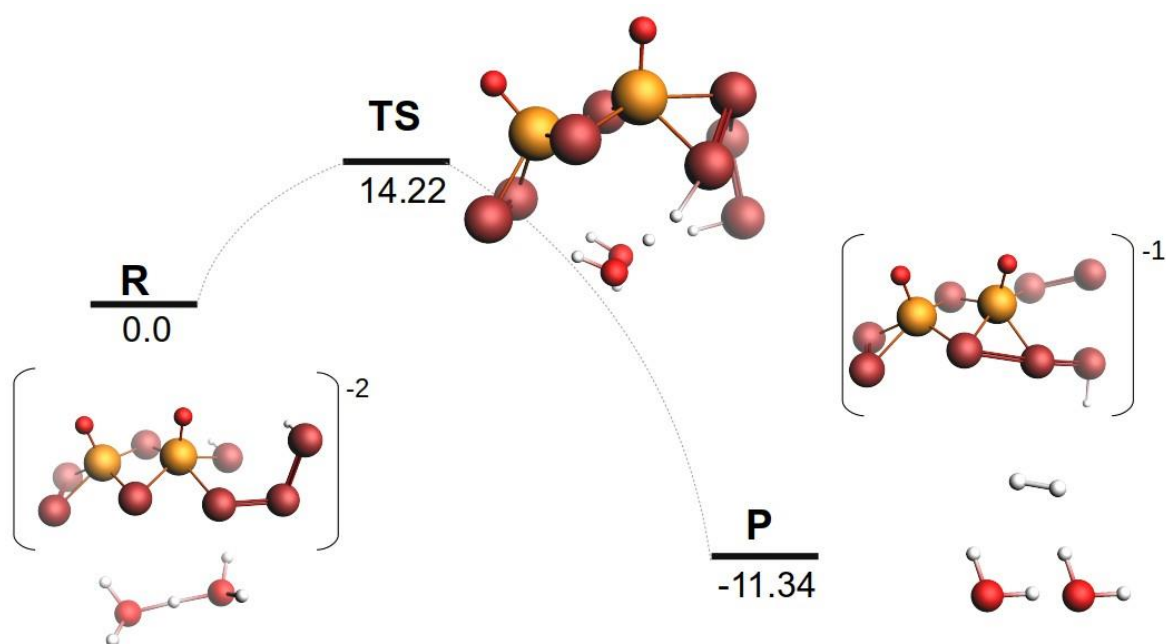
Species  $[\text{Mo}_2\text{O}_2(\mu\text{-Se})_2(\text{Se}_2)]^{4-}$  and  $[\text{Mo}_2\text{O}_2(\mu\text{-Se})_2(\text{Se}_2)(\text{Se}_4)]^{4-}$  have not large differences in their HER reaction profiles. In both cases Heyrovsky mechanism is the most favoured one based on energetic grounds. In both cases hydrogen evolution reaction from the single-protonated forms are the preferred ones.



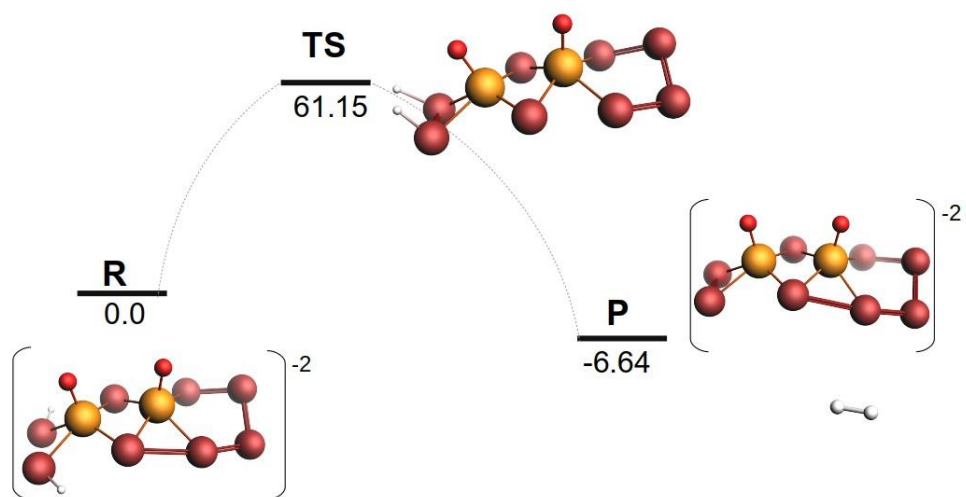
**Figure S23** Gibbs reaction profile for **Heyrovsky reaction** mechanism from single- protonated intermediate **B3**  $\text{H}[\text{Mo}_2\text{O}_2(\mu\text{-Se})_2(\text{Se}_2)(\text{Se}_4)]^{3-}$  and  $\text{H}_5\text{O}_2^+$  to  $[\text{Mo}_2\text{O}_2(\mu\text{-Se})_2(\text{Se}_2)(\text{Se}_4)]^{2-}$  and  $\text{H}_2$ .



**Figure S24** Gibbs reaction profile for **Heyrovsky reaction** mechanism from intermediate **BB1**  $\text{H}_2[\text{Mo}_2\text{O}_2(\mu\text{-Se})_2(\text{Se}_2)(\text{Se}_4)]^{2-}$  and  $\text{H}_5\text{O}_2^+$  to B1  $\text{H}[\text{Mo}_2\text{O}_2(\mu\text{-Se})_2(\text{Se}_2)(\text{Se}_4)]^{1-}$  and  $\text{H}_2$ .



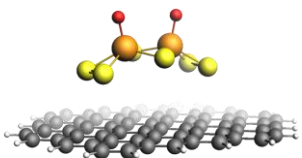
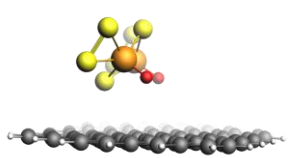
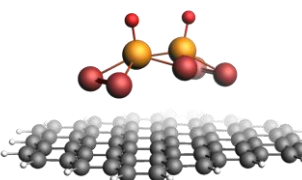
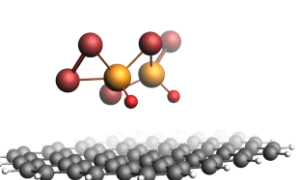
**Figure S25** Gibbs reaction profile for **Heyrovsky reaction** mechanism from intermediate **BB3**  $\text{H}_2[\text{Mo}_2\text{O}_2(\mu\text{-Se})_2(\text{Se}_2)(\text{Se}_4)]^{2-}$  and  $\text{H}_5\text{O}_2^+$  to B3  $\text{H}[\text{Mo}_2\text{O}_2(\mu\text{-Se})_2(\text{Se}_2)(\text{Se}_4)]^{1-}$  and  $\text{H}_2$ .



**Figure S26** Gibbs reaction profile for **Tafel reaction** mechanism from intermediate **BB1**  $\text{H}_2[\text{Mo}_2\text{O}_2(\mu\text{-Se})_2(\text{Se}_2)(\text{Se}_4)]^{2-}$  and  $\text{H}_5\text{O}_2^+$  to  $[\text{Mo}_2\text{O}_2(\mu\text{-Se})_2(\text{Se}_2)(\text{Se}_4)]^{2-}$  and  $\text{H}_2$ .

## Effect of electrode on energies

In this work we take molecular metal chalcogenides as a model systems. Water solvent environment was modelled with a continuous polarizable model. In the case of the electrode, we inspected the effects of electrode modelling  $\text{Mo}_2\text{O}_2(\mu\text{-S})_2(\text{S}_2)_2]^{2-}$  and  $\text{Mo}_2\text{O}_2(\mu\text{-Se})_2(\text{Se}_2)_2]^{2-}$  supported on a graphene slide model of 86 atoms. Both systems present several binding modes to graphene, being 6S most stable one for  $\text{Mo}_2\text{O}_2(\mu\text{-S})_2(\text{S}_2)_2]^{2-}$  and 3S\_2O the most stable one for  $\text{Mo}_2\text{O}_2(\mu\text{-Se})_2(\text{Se}_2)_2]^{2-}$  see Figure S23. In the case of  $\text{Mo}_2\text{O}_2(\mu\text{-Se})_2(\text{Se}_2)_2]^{2-}$  one bridging and one 2-ring selenium for each molybdenum are free to interact with protons and promotes HER mechanisms.

Binding Mode	6S	3S_2O
Energies $\Delta E$	0.0	3.70
$\text{Mo}_2\text{O}_2(\mu\text{-S})_2(\text{S}_2)_2]^{2-}$		
Energies $\Delta E$	2.48	0.00
$\text{Mo}_2\text{O}_2(\mu\text{-Se})_2(\text{Se}_2)_2]^{2-}$		

**Figure S27** Binding models of  $\text{Mo}_2\text{O}_2(\mu\text{-S})_2(\text{S}_2)_2]^{2-}$  and  $\text{Mo}_2\text{O}_2(\mu\text{-Se})_2(\text{Se}_2)_2]^{2-}$  to graphene. Relative energies in kcal/mol.

In the case of non reduced  $\text{Mo}_2\text{O}_2(\mu\text{-Se})_2(\text{Se}_2)_2]^{2-}$  compound 1 analysis of the HOMO, LUMO and lowest unoccupied LU metal complex orbital shows that there are not mixing between graphene and metal-complex frontier orbitals (see figure S24). The computed GAP for compound 1  $\text{Mo}_2\text{O}_2(\mu\text{-Se})_2(\text{Se}_2)_2]^{2-}$  deposited on 1 layer of graphene of between HOMO and LU-metal- is of 1.758 eV, almost equal to the same computed value of 1.785 eV of compound 1 in water.

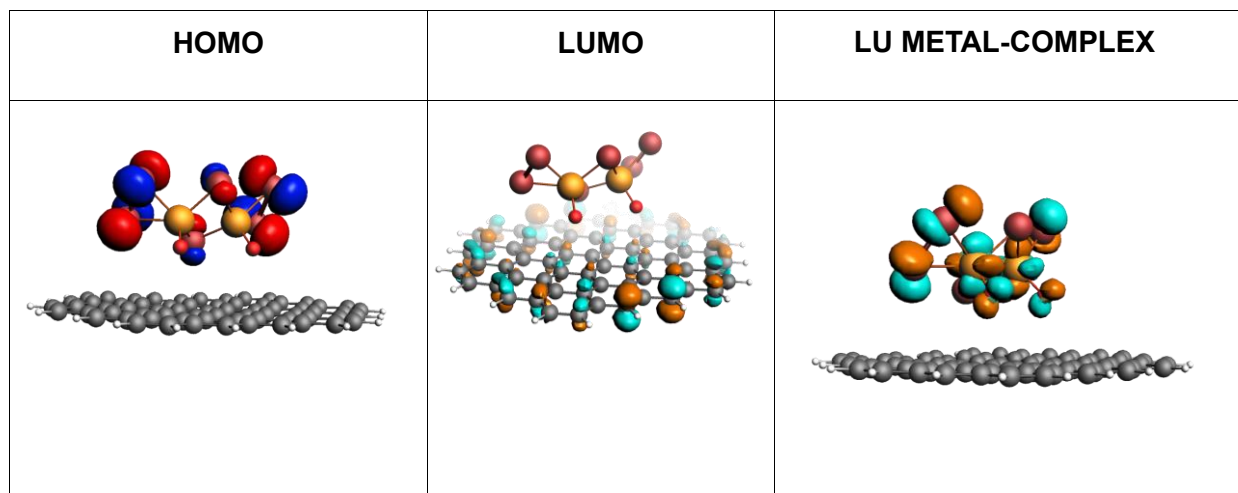


**Figure S28** HOMO and LUMO orbitals of  $\text{Mo}_2\text{O}_2(\mu\text{-Se})_2(\text{Se}_2)_2]^{2-}$  compound 1 in non-reduced form. Computed HOMO-LUMO Metal-Complex GAP = 1.758 eV.